Structural foliations from gravity gradient data for a 2D fault

Conference Paper · October 2014

DOI: 10.13140/2.1.3440.0006

2 authors:

Desmond James FitzGerald

Intrepid Geophysics, Australia

65 PUBLICATIONS **172** CITATIONS

SEE PROFILE

Horst Holste

Aberystwyth University

59 PUBLICATIONS **481** CITATIONS

SEE PROFILE

Practical demonstration of deriving structural foliations from gravity gradient data for 2D faults

D.J.FitzGerald[1] and H. Holstein[1,2], [1]Intrepid Geophysics, [2]Aberystwyth University

Summary

Gravity gradient data from a horizontal traverse over a semi-infinite 2D fault can be highly informative of the fault parameters. We present the theory for an inversion technique for recovering the parameters from the data. We follow with a case study from Nevada, where the theory is tested and adapted to cope with an actual survey.
Rapid estimates of the dip, strike, fault block tilt, depth extent of the idealized fault and the mean location of a "Hot Spot" can be practically found, provided there is a region of 400m or more where the fault signature dominates the measured gradients. The question of finding suitable sampling sites for a determination is discussed, using a clustering method and a multi-scale edge detection method. The performance of Free Air vs terrain corrected signal is also discussed in the context of interpretation.

The neglected topic of rotational errors in the tensor survey data is also raised, as so far, no practical methods have been proposed to calibrate and test for this issue. Scope exists for significant improvement in survey data and also in transforming tensor observations along profiles to extract meaningful geological observations. As fault surfaces can then be generated, independently of any seismic observations, interpreting 2D seismic data will benefit from any contributed non-vertical faults.

Introduction

The McGrath (1991) algorithm has been the starting point for this work. This is based on a simple 2-dimensional infinite body model of a sloping fault contact. Gravity profile data that cross a fault can be used to estimate the dip, block thickness and density contrast across the structure. The strike is found using standard edge detection methods. An upward continuation strategy, with uniform increments of say 5 km, is applied more than 5 times.

Gravity gradient data has richer information content, permitting parameter estimation without the need for upward continuation. Rather than a manual system based upon just one profile of gravity data, we have chosen to work on an observed tensor grid of gradient measurements, identifying possible 2D features and then sampling the grid onto a profile at regular intervals. Initially, graphical plots of the tensor components were transformed to a local reference frame at right angles to the interpreted fault structures. The newly developed theory for interpretation is presented and then tested on real data from the Montezuma prospect in Nevada, Mataragio and Hogg, 2011. The companion paper to this one is FitzGerald & Holstein 2014.

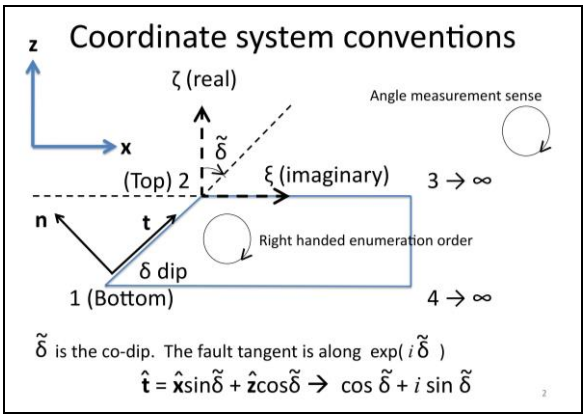

Figure 1. Fault geometry and reference systems.

Theory

A schematic view of the fault geometry under consideration is given in Figure 1. The fault is infinite in the strike direction (into the paper). It may be thought of as having a quadrilateral cross-section with vertices 1-4, in which vertices 3 and 4 take limiting positions at $x=+\infty$. The fault dip angle is δ. We find it convenient to express formulae in terms of the co-dip angle $\tilde{\delta} = \pi/2 - \delta$, which represents the deviation of the fault's edge from the vertical in the range $(-\pi/2, \pi/2)$. Equations for the gravity gradient of a target of finite polygonal cross-section have been given by Jia and Meng (2009) and by Jia and Wu (2011). We have adapted these equations for the limiting infinite cross-section. When the fault top and bottom surfaces are aligned with the *x*-axis, the infinite strike is along the *y*-axis and the *z*-axis is oriented upwards, the only non-zero components of the gravity field gradient tensor **T** are given by

$$T_{xx} = -T_{zz} = 2G\rho c\,(-c\Delta\theta + s\log(r_2/r_1)) \quad (1)$$

$$T_{xz} = T_{zx} = 2G\rho c\,(s\Delta\theta + c\log(r_2/r_1)) \quad (2)$$

where r_1 and r_2 are the magnitudes of the position vectors from the observation point to fault vertices 1 and 2 respectively, $\Delta\theta$ is the angle between them, *c* and *s* are the cosine and sine of the co-dip respectively, ρ is the density contrast, and *G* is the constant of universal gravitation.
The equations can be reorganized into a complex form that reflects the physical fault geometry more intuitively. Using $(c+is) = \exp(i\tilde{\delta})$ and polar expressions for the positions of vertices 1 and 2 as $r_1\exp(i\theta_1)$ and $r_2\exp(i\theta_2)$ respectively, with $\Delta\theta = \theta_2 - \theta_1$, equations (1) and (2) reduce to

Structural foliations from gravity gradient data for a 2D fault

$$T_{xx} + iT_{xz} = 2G\rho c\,(i\Delta\theta + \log(r_2/r_1))ie^{-i\tilde{\delta}} \quad (3)$$

$$= 2G\rho c \log(r_2 e^{i\theta_2}/r_1 e^{i\theta_1})ie^{-i\tilde{\delta}} \quad (4)$$

$$= 2G\rho c \log((z_2 + i(x_2 - x))/(z_1 + i(x_1 - x))ie^{-i\tilde{\delta}}. \quad (5)$$

The last step replaces the polar form of the vertex positions vectors in the Argand diagram by corresponding Cartesian coordinates, $((x_1 - x), z_1)$, $((x_2 - x), z_2)$, coordinates of the observation point being $(x,0)$. The five fault parameters x_1, z_1, x_2, z_2 (these also define $\tilde{\delta}$, $c = \cos\tilde{\delta}$), and ρ are now all made explicit in formulation (5). For inversion, a more convenient set of parameters is the semi-length L of the fault edge, the co-dip $\tilde{\delta}$, the combination $\Gamma = 4G\rho c$ and mean fault coordinates $\bar{x} = (x_1 + x_2)/2,\ \bar{z} = (z_1 + z_2)/2,$. The fault coordinates can be recovered via

$$z_1 + i\,x_1 = \bar{z} - Le^{i\tilde{\delta}} \quad (6)$$

$$z_2 + ix_2 = \bar{z} + Le^{i\tilde{\delta}} \quad (7)$$

Equation (5) can now be compactly written as

$$T_{xx} + iT_{xz} = \Gamma \operatorname{arctanh}\left(\frac{Le^{i\tilde{\delta}}}{\bar{z} - i(x - \bar{x})}\right) ie^{-i\tilde{\delta}} \quad (8)$$

In this form, the spatial coordinates can be solved by applying the tanh function as the inverse of the arctanh function. We obtain

$$\frac{\bar{z}}{L} = \Re\left\{\frac{-e^{i\tilde{\delta}}}{\operatorname{arctanh}\left(ie^{i\tilde{\delta}}(T_{xx} + iT_{xz})/\Gamma\right)}\right\} \quad (6)$$

$$\frac{x - \bar{x}}{-L} = \Im\left\{\frac{-e^{i\tilde{\delta}}}{\operatorname{arctanh}\left(ie^{i\tilde{\delta}}(T_{xx} + iT_{xz})/\Gamma\right)}\right\}. \quad (7)$$

When the arctanh argument has a value much less than one at positions x remote from the fault, these relations simplify to

$$\frac{\bar{z}}{\Gamma L} = \frac{T_{xz}}{(T_{xx})^2 + (T_{xz})^2} \quad (8)$$

$$\frac{x - \bar{x}}{-\Gamma L} = \frac{T_{xx}}{(T_{xx})^2 + (T_{xz})^2}. \quad (9)$$

We now apply equations (6)-(9) to deduce the fault parameters in a synthetic case.

A synthetic case study

For a given set of 5 fault parameters, equation (8) permits calculation of the gravity field gradient components along a traverse, x being the distance along a horizontal traverse. This led to Figure 2.

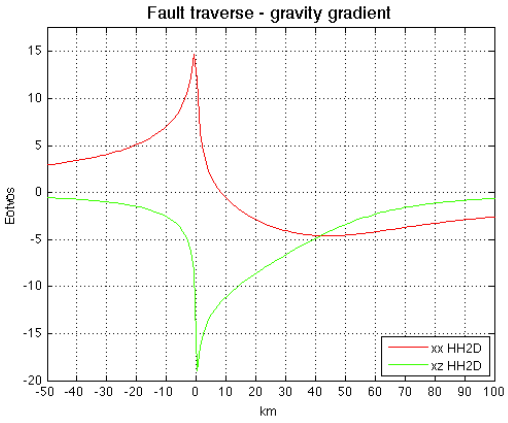

Figure 2. Components xx and xz from a horizontal traverse.

We now take the calculated tensor components synthetic observed data, and attempt to deduce the fault parameters. Equations (9) suggests that a plot of the right hand component combinations against the traverse distance x should result in a straight line of slope -1/(ΓL) and zero crossing at $x = \bar{x}$. From Figure 3, we deduce that $\Gamma L = 4G\rho cL \times 10^9$ =219E km, and $\bar{x}$ = 22km. Equation (8) predicts a horizontal asymptotic line, which is found at a level of -0.075E^{-1} = $\bar{z}/(\Gamma L)$, leading to $\bar{z} = -0.075 \times 219$ = -16 km.

The post-multiplicative factor in equation (8) suggests that a *xx*-*xz* plot is subject to a rotation by the co-dip angle, and is indeed found to be the case. Figure 4 shows such a plot, indicating a co-dip of -54 degrees. The scale and openness (eccentricity) of this curve is governed by the values of Γ and $\bar{z}/L$ in equation (8).

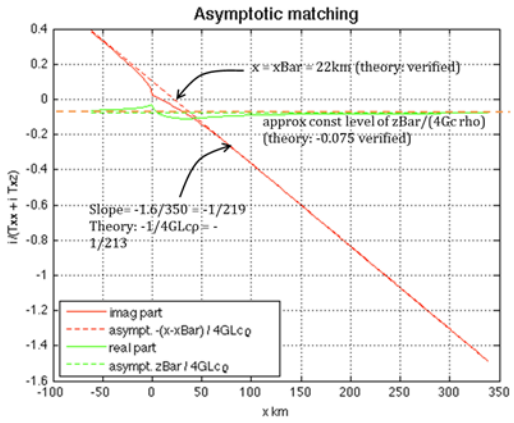

Figure 3. Components *xx* and *xz* from a horizontal traverse

Structural foliations from gravity gradient data for a 2D fault

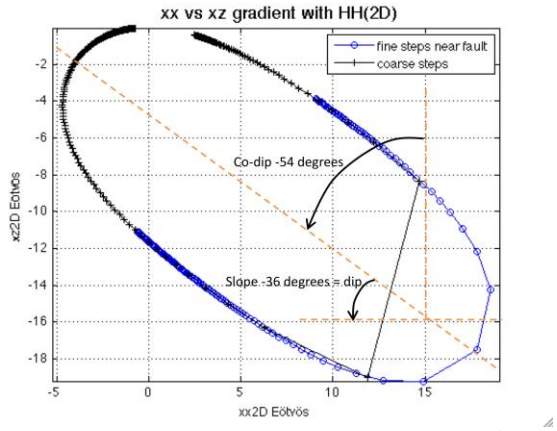

Figure 4 Components *xx* and *xz*, plotted against each other, form a segment of a closed oval curve, rotated by the co-dip angle.

Finding a match therefore gives these parameters. We find $\Gamma = 4G\rho c \times 10^9 = 7.85$ E. Having previously estimated ΓL=219E km, we obtain L=27.9 km and $\rho = \Gamma/(4Gc)$=50 SI. All these values are within 1 per cent of the model parameters.

When the correct parameters are obtained, equations (6) and (7) lead to straight line relationships when plotted against the traverse distance *x*. These equations therefore serve to finalise best parameter fits. The best fits must minimize the dispersion of data points to the theoretical straight lines. Figure 5 shows the dispersive sensitivity of the parameters in relation to their optimum values.

Case Study - Montezuma Faults

The available Bell survey data contained the components of both observed Free Air gravity gradients and a terrain corrected signal. These are combined into a tensor field and gridded, so that a tensor grid could be interrogated by estimating what the measured signal along any arbitrary profile line. This requires an underlying toolkit that is capable of all the necessary dynamic interpolation of the tensor signal, solving the Eigen System, clustering and visualization (eg Intrepid). Figure 6 shows a tensor phase pseudo-color image that is histogram equalized. This enhancement was chosen, as it shows the main rift features most starkly, namely the N20W Nevada trends and the NE cross-fault. The near linear features are easily identifiable.

Free Air vs Complete Bouguer

It can be argued that the measured Free Air signal is a good place to start when looking for near surface geology, as most fresh rock geology also has a topographic expression. Also, as approximately 80% of the measured FTG signal derives from the topography, more success might be expected. In this particular case, the reverse proved to be the case, with terrain corrected signal being used predominately for all the workings. Perhaps there is extensive weathering and older terrain that masks the near surface geology.

Automating Fault Detection

We start the localization of the search for faults by using two methods.

- The usual traditional 2D geophysics method of finding the edges by looking for the maximum of the Txz and Tyz, combined into a Total Horizontal Gradient (THG, worm_strike).
- Solving the local Eigen System for each cell in the tensor grid, and when a 2D feature is indicated by the middle eigenvalue being close to zero, capturing the properties in a point's database. An anisotropic clustering algorithm is then used to locate each cluster center, for the purpose of finding the fault properties.

The eigenvectors can be thought to carry a horizontal strike (tensor_yaw) and also a tilt angle (tensor_pitch), in a plane at right angles to the strike direction. The tilt angle represents the non-horizontal angle of the top surface of the fault block. An analysis for this survey shows most features of a 2D nature have tilt angles less than 10 degrees, with the mean below 5 degrees from the horizontal. This is discussed further below.

The presence of 2D signal dominated patches, as defined by these clusters, really means that there are no other geological features in the close proximity, that interfere with the gravity response. It does not mean that the 2D features only occur at these locations.

Profile Calculation

Table 1 shows an example of transformed tensor observations from a profile across the fault. Shown in this table are all the necessary columns to form the ellipsoid, and estimate the starting values for the mean location from the Txx vs X and Txz vs X curves. In this case the cell size is 40m, and as few as 10 observations still allow a good fit to the ellipsoid. So as long as there are no significant interfering density anomalies within 400m to the calculation site, multiple estimates can be made along the suspected fault lines. Interestingly, the eigensystem solution starts to diverge from a 2D body towards 400 meters away from the starting point, whereas, the transform along the profile direction is more stable.

The following is the result for the data in Table 1.

Mean XX, XZ (-10.828, 30.319)
Major, Minor Axis (35.241, 28.728)
co-dip, LH from +X 5.73901 radians,
dip -31.2 degrees,
strike 24.5
Number of observations 19
Number of unknowns 5
Degrees of freedom 14
Iterations until convergence 10
Variance 0.0471
Std. dev. observation unit weight 0.2169
Mean Hot spot fault location (-48.766, 1303.273) m

Structural foliations from gravity gradient data for a 2D fault

Having established that the theory seems to work in practice, the next step is further automation, with many estimates of the fault parameters, to get some experience with the variability of the method, and hence what might be required to deduce overall best estimates for a fault network geometry in 3D.

Ambiguity and Errors

A big reduction in ambiguity for potential field gravity data is demonstrated in this work, once the Full Tensor gradients are available. The reduction is the demonstrated ability to detect and map areas in your geology where there is a dominant 2D structure. Figure 7 shows a greyscale Gz, the traditional "worms" derived from Gxz & Gyz as white lines, and the 2D body zones, with coloured local strike vectors. Not all the indicated worms are supported as 2D bodies by the tougher FTG criteria.

The question of gradiometry measurement errors is also more complex than one might first suppose. The traditional approach is to look strictly at the magnitudes of the gradients, perhaps in frequency space, and to quote a noise figure such as 3 Eotvos / root Hz. All rotational errors are commonly ignored.

The 2D profile method is quite stable for any one set of numbers. The estimated result for dip is directly dependent upon the least squares fit to the ellipsoid, and the original determination of a profile direction at right angles to the dominant structural direction. Initially, the traditional THG strike was used. This varies at times more than 20 degrees from the eigenvector direction, at the same location. As we have measured gradients, the eigenvector method is judged the superior method, as it uses all the curvature gradients.

The estimation of the "mean Hot spot" location comes from the 2 trend plots of Txx and Txz, and their gradients. This has a higher error bar than the dip calculation.

Repeat tests along the 2D structure at 100m intervals, is thought to be the best way to characterize repeatability of the dip estimation process, and provided the dip of the 2D structure does not itself vary too much. Table 2 comes from the same general area as Table 1 results, but is found by moving the profile along the fault every 100m, attempting this for 4 km. Only those profiles that register a result are presented. Six of the profiles present a close result for estimates of the 2D fault properties.

Turing to the tilt angle, there is almost no discussion about the preparation of AGG data by the contractors, when it comes to measuring and removing any systematic error due to rotations of the measurement platform. Great reliance is placed upon the stabilized platforms keeping the measurement surface horizontal. All the rotations are therefore more or less accounted for, thus alleviating the need to bring these to account in the downstream processing. In our opinion, these errors get smoothed out of the delivered data. Figure 8 shows the tilt surface, derived from the 2D geology indicative cells, using an implicit function interpolation of the located strike/tilt estimates. This is after the terrain correction has been applied to the survey data.

The Kauring test range is used to compare both ground and airborne gradient data. This Nevada case study highlights the possibility of designing a test range practice to include estimates of the rotational error in the measured signal. Discussions have started to include the biggest single gravity 2D feature in Australia, as part of the test range – the Darling Fault, on the edge of the North Perth Basin.

The tilt of the 2D geology bodies in this study, rather than being horizontal, as assumed, comes in around 1 to 2 degrees. This is systematic in the measurements. The question can be put "Is this real or is it part of an uncorrected systematic acquisition error?". When we have known large 2D geological structures, field mapping can ascertain exactly what both the dip and tilt of each structure is, thus leading to the possibility of finding further ways to reduce noise in the signal, by improving the knowledge of the rotational state of the instrument in time and better processing. In the case of Kauring, almost nothing is still known of the geology, and what is known is that the geology does not contain any useable 2D structures. It is thus unsuitable as a test range for gradiometry rotational error determination.

Application Step

In the companion overview paper, there is a short description of how to use implicit function technology to generate the fault surfaces from foliation and contact observation. The fault network might not be as extensive as that indicated by traditional working, but what is presented has more robust work to support it.

Potentially, all existing AGG surveys, that have captured the Full tensor, can now be reprocessed for this extra information.

These surfaces are independent of any seismic observations, and so become a powerful aid in interpreting 2D seismic data, especially for any contributed non-vertical faults. The reason for this statement is that the velocity model, used for depth conversions, now has access to another independent means for checking, especially in the near surface region.

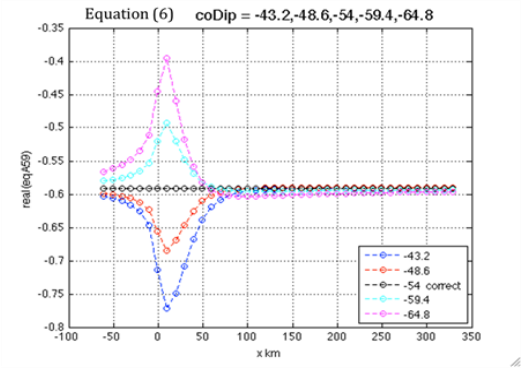

Structural foliations from gravity gradient data for a 2D fault

Figure 5 Deviation from expected horizontal straight line for non-optimum co-dip parameter values.

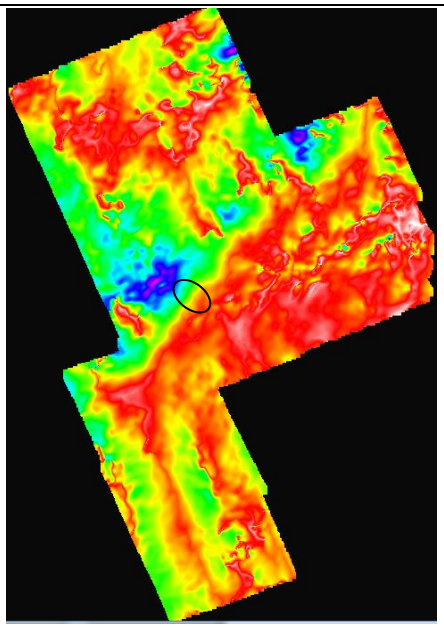

Figure 6 Montezuma gridded tensor data with a phase enhancement derived from rotating each tensor to solve the Eigen system (hence like an AGC filter). The NE cross-cutting fault and the N20W rift bounding faults are clear. Ellipse shows approximate working point for most of this study.

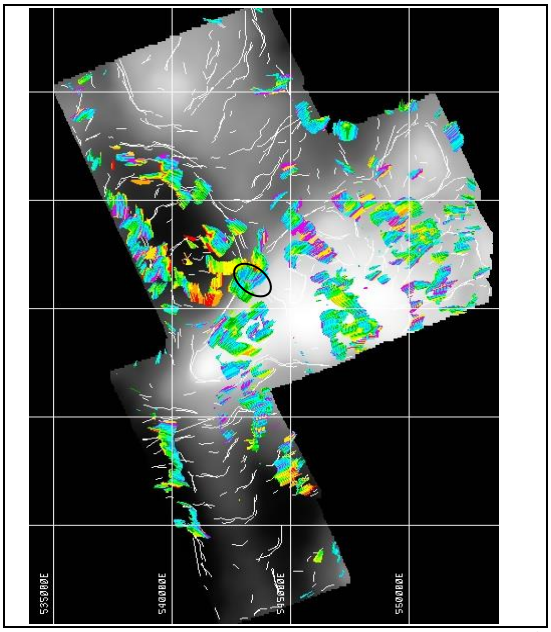

Figure 7 Montezuma vertical gravity greyscale, 3 levels of upward continued multiscale edge picks or worms, and the full tensor eigensystem derived strike vectors, showing the zones where a 2D signal character dominates the observed signal.

Gxx	Gxz	Gyy	distance	-Gxx/Gxz	Gxx_scal	Gxz_scale	x	y	XX_XZ_G	THDstrike	Yaw	Tilt	Mid eiger
10.63	50.42	0.74	-200	-210.811	0.004	0.01899	542600	4475883	51.5	21.6	22.23	-9.3	-0.017
8	51.99	0.326	-160	-153.928	0.00289	0.01879	542636.4	4475866	52.6	21.9	23.17	-9.17	-0.247
5.2	53.68	-0.226	-120	-96.8279	0.00179	0.01846	542672.8	4475850	53.9	21.9	23.83	-9.22	-0.724
2.56	55.62	-0.099	-80	-45.9421	0.00082	0.01794	542709.2	4475833	55.7	21.5	23.83	-8.98	-0.652
-0.59	57.46	-0.031	-40	10.21682	-0.00018	0.0174	542745.6	4475817	57.5	21.4	24.12	-8.54	-0.537
-4.17	58.83	0.09	0	70.96709	-0.0012	0.01691	542782	4475800	59	21.6	24.67	-8.12	-0.293
-8.31	60.26	0.334	40	137.9018	-0.00225	0.01628	542818.4	4475783	60.8	22.1	25.51	-7.61	0.161
-12.94	60.99	0.445	80	212.2416	-0.00333	0.01569	542854.8	4475767	62.3	22.8	26.56	-7.18	0.52
-18.05	60.85	0.443	120	296.6128	-0.00448	0.0151	542891.2	4475750	63.5	23.6	27.87	-6.85	0.836
-23.17	60.42	0.255	160	383.5356	-0.00553	0.01443	542927.6	4475734	64.7	24.8	29.48	-6.3	1.081
-28.09	58.46	-0.011	200	480.5832	-0.00668	0.0139	542964	4475717	64.9	26.2	31.19	-5.7	1.306
-33.93	55.99	-0.322	240	605.9515	-0.00792	0.01306	543000.4	4475700	65.5	27	32.88	-5.48	1.57
-38.03	52.44	-0.582	280	725.2126	-0.00906	0.0125	543036.7	4475684	64.8	26.4	33.67	-5.7	1.559
-41.47	47.76	-0.789	320	868.2538	-0.01037	0.01194	543073.1	4475667	63.2	24.5	34.44	-6.36	1.56
-43.56	42.96	-0.586	360	1013.92	-0.01164	0.01148	543109.5	4475651	61.2	22.1	35.03	-7	1.849
-44.31	38.18	-0.386	400	1160.405	-0.01295	0.01116	543145.9	4475634	58.5	18.8	35.52	-7.68	2.016
-44.42	34.4	-0.014	440	1291.537	-0.01407	0.0109	543182.3	4475617	56.2	15.6	35.89	-8.18	2.328
-44.08	31.34	0.602	480	1406.251	-0.01507	0.01072	543218.7	4475601	54.1	11.9	36.13	-8.88	2.829
0	0	0											

Table 3: Montezuma Transverse Fault. A profile is sampled across the fault, centred at distance zero to the best starting location.

A prior step chooses the likely fault point, then estimates the average fault strike as 24.5. The profile is strike 114.5 with a fault block tilt estimate at -8.4 degrees. Points in the table are constrained so that Gyy be less than 1 Eotvos along the profile and the vertical profile plane Total gradient (Txx,Txz) is greater than 15 Eotvos. These points are then feed directly into the ellipsoid fitting routine.

Conclusions

This work generalizes the approach by McGrath to determine fault parameters from gravity data. In our case we have access to gravity gradient data, and demonstrate its rich information content, permitting parameter estimation without the need for upward continuation. Rapid estimates of the dip, strike, fault block tilt, depth extent for an idealized fault and the mean location of a "Hot Spot" can be practically found, provided there is a region of 400m or more where the fault signature dominates the measured gradients. Clustering, using an anisotropic, recursive technique is also quite effective at finding sites suitable for dip determination. The best automatic performance so far, with this dataset, is to get 25% successful dip calculations from the cluster approach. Further improvements in the clustering algorithm are possible. The "worming" approach is not quite as successful, as there is no guarantee that a suitable site for the dip determination will be found, while traversing the indicated edge (say 12% success). Repeatability of the estimate for dips to +/- 5 degrees or better is shown, along a structure that is showing a high degree of 2-Dimensionality, once you have identified suitable test sites. All previously acquired Full tensor Gravity gradiometry surveys can be processed, to find better control on 2D faults. The possibility for a new method for calibrating and correcting for FTG rotational errors also emerges from this work. This has long been ignored as a source of a systematic error that could be removed. As this survey was acquired over 6 years ago, there have been continual improvements in acquisition practice, so 2D geological structures with more subtle signatures will likely also be found by adjusting the noise floor of 2 Eotvos and a minimum of 15 Eotvos for the in plane total gradient.

Acknowledgments

James Mataragio from Bell Geospace, and John Hogg of CMQ are thanked for access to the geophysical and geology data from Nevada. For those wishing to replicate or check this work, data access should be possible.

REFERENCES

FitzGerald, D., and H. Holstein, 2014, Structural geology observations derived from full tensor gravity gradiometry over rift systems*:* 84th SEG Annual meeting, Expanded Abstracts.

Fitzgibbon, A. W., M. Pilu, and R. B. Fisher, 1999, Direct least-squares fitting of ellipses: 21, 476–480.

Jia, Z., and L. Meng, 2009, Magnetic gradients produced by a 2d homogeneous polygonal source.: Geophysics, 74, L1– L6.

Jia, Z., and S. Wu, 2011, Potential fields and their partial derivatives produced by a 2d homogeneous polygonal source: A summary with some revisions: Geophysics, 4, L29–L34.

Mataragio J., and J. Hogg, 2011, Identifying prospective areas for sediment- and volcanic- hosted gold deposits using Full Tensor Gravity Gradiometry: 12th International Congress of the Brazilian Geophysical Society held in Rio de Janeiro, Brazil, August 15-18.

McGrath, P.H., Dip and depth extent of density boundaries using horizontal derivatives of upward-continued gravity data. Geophysics, 56, 1533-1542,6

X	Y	Depth	dip	strike	tilt
542620.2	4475958	1058.8	73.6	44.2	-5.8
542578.2	4475992	1011.2	72.5	43.3	-4.7
542559.6	4475994	923.2	87.7	41	-3.3
542583.2	4475966	1012.5	76.5	39.8	-4.2
542598.7	4475953	1047.2	77.5	39.8	-4.8
542597.5	4475952	1048.8	77.1	39.5	-4.7
542764.1	4475808	1487.1	-34	25.2	-9.7
542731	4475824	1308.5	-31.3	24.9	-7.9
542641.2	4475847	1089.9	-10.6	18.3	-2.5
542609.5	4475856	993	-8.5	18	-1.2

Table 2: Montezuma Transverse Fault. Semi-parallel profiles at 100m intervals along the fault to test repeatablility and stability of hot spot location, dip and tilt estimation. First 6 results quite acceptable. Last 4 estimates are less reliable – near the edge of the 2D zone.

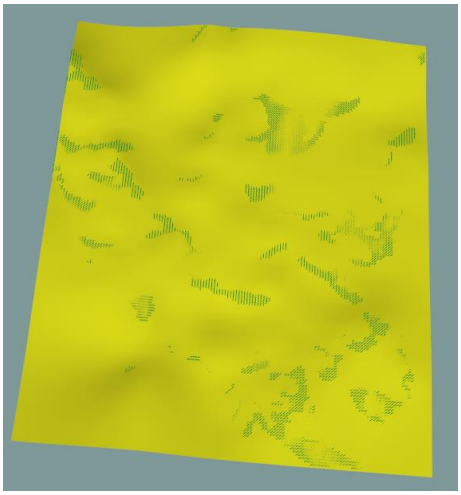

Figure 8 Montezuma tilt surface, derived from the 2D geology indicative cells. This is after the terrain correction has been applied to the survey data.